A Novel Continuum Manipulator Design Using Serially Connected Double-Layer Planar Springs

Peng Qi, *Student Member, IEEE*, Chen Qiu, Hongbin Liu, *Member, IEEE*, Jian S. Dai, *Senior Member, IEEE*, Lakmal D. Seneviratne, and Kaspar Althoefer, *Member, IEEE*

***Abstract*—There is a surge of research interest in the field of "continuum robotics." Robots created under this paradigm offer many advantages and represent unique features in terms of flexibility, dexterity, safety, and weight reduction. This paper introduces a novel continuum manipulator that integrates multiple layers of compliant planar springs—a structure that provides several notable advantages over existing designs. First, it possesses precise linear large-displacement motion. In this context, we utilize the linear output motion of each layer of springs. With the serial connection of multiple conjoined layers, the manipulator demonstrates linear predictable bending even when executing large bends. An analytical method is provided to study the compliance characteristics of the planar spring and derive the compliance matrix to represent the force–deflection relationships, allowing an accurate motion prediction. Second, compared with work elsewhere, this structure demonstrates an effective way of decoupling bending from contraction and expansion. It reduces the uncontrolled compression when generating normal deflections, thus controlling robot bending is simplified. Third, the reachable workspace of the end effector is enlarged by means of varying the length of the continuum manipulator via controlled contraction and expansion. A 3-D printed prototype of this continuum manipulator is experimentally evaluated. The conducted experiments demonstrated validity of our approach.**

***Index Terms*—Compliance analysis, continuum manipulator, double-layer planar spring, tendon-driven mechanism.**

I. Introduction

CONTINUUM manipulators, inspired by elephant trunks and octopus tentacles, increasingly arouse the attention of researchers due to appealing advantages, such as compliance, dexterity, and potential for miniaturized profile. A continuum manipulator has the capability to continuously bend and theoretically possesses an infinite number of degrees of freedom (DOF). Remarkable developments in this area have been seen in the past two decades: various forms of design were created; many new applications for such continuum robots were demonstrated across different sectors, including industrial operations and health-care environments [1]. The related scientific problems range from designing and modeling continuum manipulators to low-level control and high-level task execution [2].

Historically, the first continuum manipulator is generally accepted to be Anderson and Horn's tensor arm manipulator invented in the late 1960s [3]—a tendon-driven spine-like flexible arm. Subsequently in 1971, Hirose started to propose creative designs of snake-like robots and appropriate control systems based on the biomechanical study of snakes [4]. Early works also include Chirikjian's pilot research in the 1990s on establishing the fundamental modeling technique to formulate the dynamics of hyperredundant manipulators [5]. The late 1990s and 2000s saw an increasing trend of miniature continuum manipulators being moved into robotic surgery with a view to finding solutions for robot-assisted minimally invasive surgery (MIS) with its inherent access problems through small incisions [6], [7]. Meanwhile, soft robotics as a subset of continuum robotics emerged with the development of novel soft actuators and sensors [8], [9]. Webster and Jones [10] presented a milestone review on the constant-curvature kinematics methodology of continuum manipulators and summarized the early developments. Most recently, Walker [1] reviewed the state of the art of continuous backbone robot manipulators and analyzed the hardware design principles.

A. Related Work

A continuum manipulator is characterized by its continuously bending structure. Some hyperredundant manipulators [5] have, externally viewed, the appearance of a continuum arm; however, if they are internally comprised of a segmented backbone with many short rigid links/columns, they do not represent, strictly speaking, continuum manipulators—we will refer to such manipulators as "continuum-style manipulators." The frequently applied continuum-style robot constructions to date are then summarized according to their distinctive backbone architectures. Of these design principles, the earlier robot structure is composed of serially connected independent joints, and, thus, pertains to the aforementioned hyperredundant manipulator. Examples include different kinds of snake-like robots, which are articulated by revolute joints [4], universal joints [11], [12], or spherical joints [13]. In terms of actuation mode, this type of design employs an individual micromotor per joint [12], or more commonly incorporates tendon-driven actuation [11], [13]. The designs share the advantages of having a large number of DOFs and accurate control; however, they suffer from the

Manuscript received June 3, 2015; revised September 9, 2015; accepted October 15, 2015. Date of publication November 6, 2015; date of current version April 28, 2016. Recommended by Technical Editor J. Ryu. This work was supported in part by European Commission's Seventh Framework Programme under grant agreement 287728 in the framework of EU Project STIFF-FLOP and in part by the China Scholarship Council.

P. Qi, C. Qiu, H. Liu, J. S. Dai, and K. Althoefer are with the Centre for Robotics Research, Department of Informatics, King's College London, London WC2R 2LS, U.K. (e-mail: peng.qi@kcl.ac.uk; chen.qiu@kcl.ac.uk; hongbin.liu@kcl.ac.uk; jian.dai@kcl.ac.uk; kaspar.althoefer@kcl.ac.uk).

L. Seneviratne is with the Khalifa University, Abu Dhabi, UAE, and also with the King's College London, London WC2R 2LS, U.K. (e-mail: lakmal.seneviratne@kustar.ac.ae).

Color versions of one or more of the figures in this paper are available online at http://ieeexplore.ieee.org.

Digital Object Identifier 10.1109/TMECH.2015.2498738

problems of lighter payload, joint friction, and incompressibility/inextensibility.

Perhaps the most common form of a truly continuum robot is the one that uses a spring backbone [3], [14]–[16]. Due to the flexibility of the spring structure, the shape of such a robot can be actuated in a tendon-driven manner and allows us an ideal axial compliance combined with a relatively low hysteresis. Here, tendons are routed along the spring backbone producing torques at the termination points, which give rise to an underactuated design. When forces are applied to tendons, compression and bending deflections can be obtained. However, in such robots compression and bending deflections are mechanically coupled, leading to a bending actuation that results partially in compression [1]. Similar to spring backbone design, the bending flexure joint type is an another form of constructing continuum manipulators and is often used in steerable MIS instruments [17]. These robots are made of compliant materials and the flexural parts are carved from a single piece of thin-walled shell allowing bending. This structure essentially acts like springs but suffers from poor bending performance, which strongly depends on the flexure joint and material properties. One main advantage of using this design is a large open lumen within the metal shell.

Another popular design of continuum robots utilizes a laterally superelastic, but longitudinally incompressible rod/tube as the backbone element. This continuous backbone design is commonly wire actuated [18]; however, there are exceptions from this rule, in which case, the wires are replaced by a secondary backbone and bending is achieved by means of a push–pull mode [19]. A distinctive feature of using an elastic central backbone is design simplicity. On top of this, both control and modeling will be simplified. Some commonly used medical devices share this feature as well, in [20], for example, a catheter is introduced, which can be seen as an elastic tube steered by tendons. Furthermore, a multisection design emerged, producing S-shape and more complex configurations. The following is a special case of a continuum manipulator, known as active cannula or concentric tube, proposed by Webster *et al.* [21], [22] and Dupont *et al.* [23]. The main idea is to utilize precurved superelastic tubes to achieve various backbone shapes. The bending of a continuum manipulator can be formulated by beam-mechanics-based models. More recently, the ideas of layer jamming [24] and granular jamming [25] have been exploited to achieve tunable stiffness of the continuum robot structure. They differ from previous designs being composed of multiple jamming elements. The structure stiffness is changed by applying vacuum pressure to control the friction between granular media.

Except for the aforementioned types of continuum manipulators that employ different modalities of a backbone structure, there is also the "invertebrate" design. It is often termed as "bioinspired soft continuum robot." In this case, continuum manipulators are integrated with artificial muscles but do not possess a backbone or spine [26], [27]. The designs directly resemble animals or animal appendages, for example, octopus tentacles; different actuation mechanisms are used. Most often, continuum structures are pneumatically actuated—an approach closest to a muscular hydrostat [28]. That not only enables the robot to achieve elongation/shortening and bending motions, but also provides the capabilities of stiffening and force generation. Recent advances in both soft actuators and sensing techniques have led to an increased interest in the use of soft structures in continuum manipulators; however, it is still an inchoate field and a number of fundamental scientific issues need to be addressed. In particular, the fabrication and control of soft bodies would be challenging. It is expected that this kind of continuum manipulators embodies new robotic concepts and leads the design of mechanisms to the essence of biological systems.

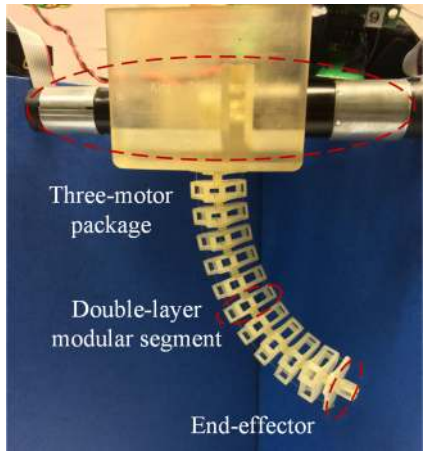

Fig. 1. 3-D printed prototype of the proposed continuum manipulator concept with multilayer deformable planar springs in series and articulated by tendons which are actuated by motors in the periphery.

So far, these fundamental, related, and broader continuum-style manipulator designs were reviewed. Nevertheless, the diversity of design strategies is not limited to the aforementioned structures. We seek to put our work in the context of other continuum manipulator designs and discuss its advantages and negative aspects. It was recognized that no single design is perfect.

B. Contribution

This paper builds on our previous work in [29], in which the early idea of designing a continuum manipulator with multilayer planar springs was introduced (see Fig. 1). This study further investigates the characteristics of the proposed manipulator and contains improvements in terms of extended content, analysis, and experimental validation. One primary advantage of using compliant planar springs is due to their linear output motion. We systematically generalize the analytical method to study the compliance characteristics of the planar spring and provide the unified compliance matrix to represent the force–deflection relationships, thus allowing us to accurately predict the robot's motion. Another advantage of the continuum manipulator is due to the serial connection of the conjoined layers; thus, allowing linear predictable bending even for large bends, although the linear-motion approximation of each individual layer only holds under the condition of small deflections. The proposed structure behaves like a helical spring, but its contraction and bending motion are decoupled, thus virtually eliminating any uncontrolled compression when generating bending deflections. Additionally, the structure is longitudinally compliant—a desirable feature in robotics, which improves safe interactions. On the other hand, the compressible manipulator length extends the achievable workspace and enhances the dexterity tuning manipulator's tip orientations.

The rest of paper is organized as follows: Section II presents the structure and design of the proposed continuum manipulator

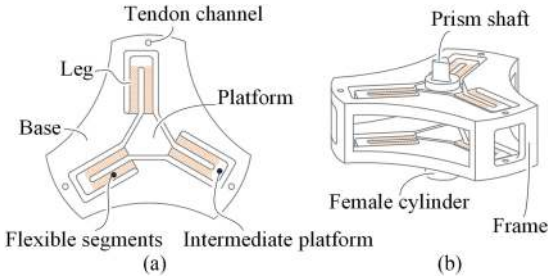

Fig. 2. Schematic of a double-layer modular segment. (a) Top view; (b) side view. The pattern-filled parts represent the flexible segments.

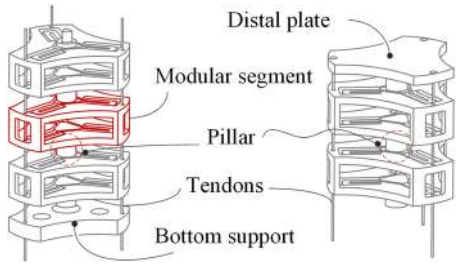

Fig. 3. Partial views of a continuum manipulator assembly.

in detail. Section III derives the symbolic formulation of compliance matrix of planar spring in the frame work of screw theory and then gives compliance analysis and numerical studies; furthermore, the finite-element analysis (FEA) simulations are provided to validate the analytical model of the compliant planar spring. Section IV provides analysis on the compliance and bending characteristics of the full robot and also an overview of the kinematics and statics. In Section V, a set of experiments are designed to evaluate the expected properties of this continuum manipulator; finally, conclusions and future works are given in Section VI.

II. Conceptual Design of the Robot

A. Segment Design

Fig. 2(a) depicts a top view of the compliant planar module. Howell *et al.* first constructed similar types of designs and identified different configurations [30] and considered them as a unique type of planar springs. We further put forward that this planar spring not only undergoes an out-of-plane motion along an axis orthogonal to the parent plane, but also has the potential for angular deflection. In Fig. 2(a), the radial-leg design is presented in detail: three legs (120° apart) radially extend away from the central platform and are anchored to the outer base; each leg has two flexible segments shaped like a "U" (U-shape design); the intermediate platform is considered infinitely stiff. In the current prototype design, the circular outer contour has a 29 mm diameter and the length of each leg is 8 mm. The thickness of the flexible beam elements is 1 mm, the width 1.2 mm, and both can be varied to change the beam compliance. Part of the base is cut in order to reduce the mass. Three tendon channels with a 0.8 mm diameter are reserved for guiding tendons through each module layer. The tendons are positioned on the far edge of the base and along the extension line of the leg. Optimization of the design is needed regarding different practical specifications and fabrication materials. Due to the elastic flexing of the slender leg beams, this compliant planar spring possesses motions to raise and lower the platform relative to the fixed base and to allow the platform to freely perform titling motions around the center. A three-legged design is chosen because having three legs is the minimum odd number leg count to allow reducing the rotational tendencies of each leg and increasing the stability of the platform [30].

Fig. 2(b) depicts the modular segment design for our continuum manipulator. It integrates two layers of compliant planar springs opposing each other; a prism-like shaft and a mating female cylinder are, respectively, fixed on each platform at the top and the bottom. The polygonal cross-sectional design of the axial coupling resists relative rotation between the two segments, while enabling torque transmission. They are fitted precisely to connect from segment to segment. This design simplifies the assembly of the current 3-D prototyped modules. Except for the flexible segments and the two platforms with their "vertebrae," any other part of the segment is a part of the frame [see Fig. 2(b)], which is idealized to be a rigid body. If fixing the bottom cylinder rigidly to the ground and applying a load to the prism shaft, the relative displacement and/or rotation of the two platforms would be double when compared to that of one layer for the same load. The gap between the two layers currently is 5 mm, providing enough space to keep the deformed legs or two platforms of the top and bottom layers, respectively, from colliding during a bending motion. The segmented modular design allows the length of the continuum manipulator to cope with various intended bending scenarios.

B. Continuum Robot Assembly

Our current continuum manipulator prototype consists of ten modular segments. Fig. 3 shows partial views of the assembly. Including a distal plate and a bottom support, the total length is 143 mm. The distance between the lower layer of one segment and the upper layer of the subsequent segment is 5 mm, and in our prototype, the same gap of 5 mm is chosen as distance between the upper and lower layers of each segment. Three tendons are routed along the aligned segments through tendon channels and secured to the distal plate, which is connected to upper layer platform of the last segment; this approach leads to a tendon-driven underactuated design. By pulling the tendons, the load will be transmitted from the distal top platform to the proximal bottom support, thus generating compression and steering motions. Moreover, depending on the intended operations, the design could be extended by incorporating additional groups of tendons to increase the mobility and functionality. The set of tendons are secured to some selected pillar and produce torques to the section down to the tendon termination point. Other continuum robots utilizing local spring elements along the backbone have appeared and been presented in [14]–[16] and [31], however these spring elements are the basic helical springs. The design features of the proposed continuum robot, in this paper, are utilizing a type of planar springs and introducing the double-layer modules.

III. Compliance of a Planar Spring

From the perspective of the mechanical design, this planar spring is a type of hybrid flexure mechanism [30]. Each flexible

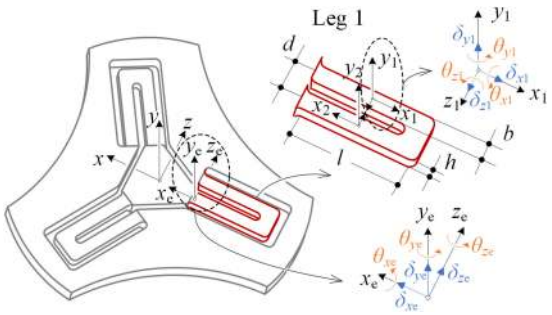

Fig. 4. Illustration of local and global coordinate frames on the planar spring plane.

segment in each leg can be treated as a beam flexure. Each leg is a folded serial chain of two fixed-guided beam flexures. This planar spring is formed by connecting the central platform to the outer base through three legs in parallel. Thus, we can stepwise derive the compliance matrix for the entire module with a bottom-up approach. Stiffness and compliance analysis for the general robots has also been represented in other different ways before [32], [33].

A. Compliance Matrix Derivation

Fig. 4 depicts the establishment of the local and global coordinate frames. The linear elasticity is considered throughout the derivation. In the framework of a screw theory [34], a small deformation of a beam is defined as a twist deflection, which in axis coordinates can be denoted by

$$\boldsymbol{S} = \begin{bmatrix} \delta_x & \delta_y & \delta_z & \theta_x & \theta_y & \theta_z \end{bmatrix}^T \tag{1}$$

where the first three elements represents the three translational deflections along their corresponding axes, while the last three elements reveal the corresponding rotational deflections. A twist deflection $\boldsymbol{S}$ is an element of the Lie algebra $se(3)$ of Lie group $SE(3)$.

In-line with (1), the loading force is considered as a general wrench in ray coordinates

$$\boldsymbol{W} = \begin{bmatrix} f_x & f_y & f_z & m_x & m_y & m_z \end{bmatrix}^T \tag{2}$$

in which the location of the axis of the wrench is given by the primary part $\boldsymbol{f} = \begin{bmatrix} f_x & f_y & f_z \end{bmatrix}^{\mathrm{T}}$, while the secondary part $\boldsymbol{m} = \begin{bmatrix} m_x & m_y & m_z \end{bmatrix}^{\mathrm{T}}$ is the vector attached with the force intensity, representing the direction of the axis of the wrench. A wrench is an element of the dual Lie algebra $se^*(3)$.

Consider one beam of the leg (see pictured in red in Fig. 4), a local coordinate frame $\{x_1 y_1 z_1\}$ generally can be established at the centroid of the beam. With the coordinates of both the twist deflection and the wrench written in the same frame $\{x_1 y_1 z_1\}$, then the compliance matrix of this beam can be derived [35] and expressed as

$$\boldsymbol{C}_1 = \mathrm{diag}\left[\frac{l}{EA} \quad \frac{l^3}{12EI_z} \quad \frac{l^3}{12EI_y} \quad \frac{l}{GJ} \quad \frac{l}{EI_y} \quad \frac{l}{EI_z} \right] \tag{3}$$

where the primary part represents linear compliance and the secondary part the torsional compliance. The beam has a length l and a rectangular cross section with the width b and the thickness $h(b > h)$. The area of the cross section is represented by A which is equal to bh, E denotes the elastic module of the material, and G denotes the shear module of the material with $G = E/(2(1 + v))$ and v being Poisson's ratio. The moments of inertia of the beam at the cross section with respect to the y-axis and z-axis are $I_y = b^3 h/12$ and $I_z = bh^3/12$, respectively, and the torsional moment of inertia is described by J.

Equivalent results are also produced in [35]–[37] and there exists remarkable similarity, however due to coordinate frame choices, they are diverse in form. The compliance of an individual link or a whole mechanism system is their intrinsic property, but the expression of the compliance matrix may vary depending on the coordinate frame choice.

For (1)–(3), we have the relations between a twist deflection and a loading wrench as summarized below

$$\boldsymbol{S} = \boldsymbol{C}_1 \boldsymbol{W}, \quad \boldsymbol{W} = \boldsymbol{K}_1 \boldsymbol{S}, \quad \boldsymbol{C}_1 = \boldsymbol{K}_1^{-1} \tag{4}$$

where $\boldsymbol{K}_1$ is the stiffness matrix in the local coordinate frame $\{x_1 y_1 z_1\}$.

The second beam of the U-shaped leg is an identical flexible segment to the first one, thus the compliance matrix is the same but expressed in its own local coordinate frame $\{x_2 y_2 z_2\}$ as shown in Fig. 4. Two beams in the leg are connected by an intermediate platform, but it is modeled as a fixed pin joint with its compliance ignored, when we consider the force–deflection relationship of the leg [30]. At the connecting edge between the leg and the platform, we established the leg global coordinate frame $\{x_e y_e z_e\}$. To shift the local coordinate frame of each beam into the global coordinate frame $\{x_e y_e z_e\}$, an adjoint action of Lie group $SE(3)$ on its Lie algebra is introduced through a 6×6 matrix representation [34]:

$$Ad_g = \begin{bmatrix} \boldsymbol{R} & \boldsymbol{0} \\ \boldsymbol{DR} & \boldsymbol{R} \end{bmatrix} \tag{5}$$

where $\boldsymbol{R}$ is a 3×3 rotation matrix representing the orientation of frame $\{x_e y_e z_e\}$, relative to frame $\{x_1 y_1 z_1\}$; in this case, $\boldsymbol{R} = \boldsymbol{R}_y(\pi)$. $\boldsymbol{D}$ is a skew-symmetric matrix spanned by the position vector $\boldsymbol{d}$ of the origin of $\{x_1 y_1 z_1\}$ from the origin of frame $\{x_e y_e z_e\}$; in this case, $\boldsymbol{d} = [-l/2,\ 0,\ d]^T$.

Then, the coordinates of a twist deflection and a wrench in the coordinate frame $\{x_e y_e z_e\}$ are calculated as [35], [38]

$$\boldsymbol{S}' = Ad_g^{-T} \boldsymbol{S}, \quad \boldsymbol{W}' = Ad_g \boldsymbol{W}. \tag{6}$$

To obtain the compliance matrix $\boldsymbol{C}_1{}'$ in the new coordinate frame, we deduct it as follows based on (4):

$$\boldsymbol{S}' = Ad_g^{-T} \boldsymbol{S} = Ad_g^{-T} (\boldsymbol{C}_1 \boldsymbol{W}) = Ad_g^{-T} \boldsymbol{C}_1 Ad_g^{-1} \boldsymbol{W}'. \tag{7}$$

Thus, we find that the compliance matrix will be transformed to the new coordinate frame according to the relation

$$\boldsymbol{C}_1' = Ad_g^{-T} \boldsymbol{C}_1 Ad_g^{-1}. \tag{8}$$

Similarly, we can derive the stiffness matrix in the new coordinate frame $\{x_e y_e z_e\}$ as

$$\boldsymbol{K}_1' = Ad_g \boldsymbol{K}_1 Ad_g^T. \tag{9}$$

Here, the inverse and the inverse transpose of such adjoint transformation matrix are given, respectively, by

$$Ad_g^{-1} = \begin{bmatrix} \boldsymbol{R}^T & \boldsymbol{0} \\ -\boldsymbol{R}^T \boldsymbol{D} & \boldsymbol{R}^T \end{bmatrix}, \quad Ad_g^{-T} = \begin{bmatrix} \boldsymbol{R} & \boldsymbol{D}R \\ \boldsymbol{0} & \boldsymbol{R} \end{bmatrix}. \tag{10}$$

If all deformations are presented into the same coordinate frame $\{x_e y_e z_e\}$, then the overall compliance matrix of the leg as a serial flexure chain is [37]:

$$\boldsymbol{C}_{l1} = \sum_{i=1}^{2} \left(Ad_g\right)_i^{-T} C_i \left(Ad_g\right)_i^{-1} =$$

$$\begin{bmatrix} \frac{2l}{EA}+\frac{d^2 l}{EI_y} & 0 & \frac{d^2 l}{2EI_y} & 0 & -\frac{dl}{EI_y} & 0 \\ 0 & \frac{2l^3}{3EI_z}+\frac{d^2 l}{GJ} & 0 & \frac{dl}{GJ} & 0 & \frac{l^2}{EI_z} \\ \frac{dl^2}{2EI_y} & 0 & \frac{2l^3}{3EI_y} & 0 & -\frac{l^2}{EI_y} & 0 \\ 0 & \frac{dl}{GJ} & 0 & \frac{2l}{GJ} & 0 & 0 \\ -\frac{dl}{EI_y} & 0 & -\frac{l^2}{EI_y} & 0 & \frac{2l}{EI_y} & 0 \\ 0 & \frac{l^2}{EI_z} & 0 & 0 & 0 & \frac{2l}{EI_z} \end{bmatrix}. \tag{11}$$

Given a compliance matrix of one leg, its corresponding stiffness matrix $\boldsymbol{K} = \boldsymbol{C}^{-1}$ is first calculated. It is noted that all twist deflections and wrenches here must be transformed into the same coordinate frame, and, correspondingly, the stiffness matrix of each leg will be expressed in such a global coordinate frame. We establish the module global coordinate frame $\{xyz\}$ in the center of the triangular platform (see Fig. 4). The radius of the plate is labeled by parameter r. The coordinate transformation operation from the connecting edge between the leg and the platform, i.e. the edge of the disc to the center of the disc follows the aforementioned relationship [see (9)]. Further considering that the overall layer's stiffness is isotropic [39], it gives the unified form as

$$\boldsymbol{K}_0 = \sum_{i=0}^{2} \boldsymbol{N}^i \boldsymbol{K}_1' \left(\boldsymbol{N}^T\right)^i \tag{12}$$

where $\boldsymbol{K}_1{}'$ is the stiffness matrix of leg 1 in the global coordinate frame $\{xyz\}$; it is derived by the relation $\boldsymbol{K}_1{}' = \boldsymbol{T}\,\boldsymbol{K}_1\boldsymbol{T}^{\mathrm{T}}$ based on (9), which indicates a coordinate transformation from the leg global coordinate frame at the connecting edge to the module global coordinate frame of the platform center. In this case, $\boldsymbol{T}$ only possesses the translation action along the x-axis. $\boldsymbol{N}$ describes the rotation action based on the fact that three legs are symmetrically connected to the platform with an angle of 120°.

Finally, the compliance matrix of the overall planar spring as a type of hybrid flexure mechanisms is computed by inverting the stiffness matrix $\boldsymbol{K}_0$

$$\boldsymbol{C}_0 = \boldsymbol{K}_0^{-1} = \mathrm{diag}\left[\begin{array}{cccccc} c_{11} & c_{22} & c_{33} & c_{44} & c_{55} & c_{66} \end{array}\right]. \tag{13}$$

Here, the nonzero compliance elements are denoted by the variables with two subscripts unnumbered equation shown at the bottom of the next page.

$$c_{11} = c_{33} = \frac{l^3\left(Ad^2+4I_y\right)}{3EI_y\left(3Ad^2+Al^2+12I_y\right)}$$

$$c_{22} = \frac{l\left(3EI_z d^3+GJl^2\right)}{18EI_z GJ}$$

$$c_{44} = c_{66} = \frac{4}{3}$$

$$\cdot\frac{l\left(EI_z 3d^3+GJl^2\right)}{EI_z GJ\left(6d^2+4l^2+12r^2-6\sqrt{3}lr+6dr\right)+\left(EI_z\right)^2 3d^2+\left(GJ\right)^2 l^2}$$

The compliance elements are all determined by both material parameters and geometric parameters of the mechanical design of the compliant planar spring structure.

B. Compliance Analysis and Numerical Example

The compliance matrix in (13) is symmetric positive definite, and the diagonal entries represent the translational and rotational compliance in/about all directions, respectively. Besides, all diagonal compliance elements of $\boldsymbol{C}_0$ can factor out a factor that coincides with the corresponding elements of beam's compliance matrix in (3). By observing compliance elements of $\boldsymbol{C}_0$, we notice that the xz planar motion (x, z, θ_y) is decoupled from out-of-plane forcing and vice versa. On the other hand, the entries outside the main diagonal are all zero, revealing that the out-of-plane rotation and translational motion of the platform are decoupled. This further verifies that the contraction effort and bending motion of the multilayer structured continuum manipulator will be theoretically independent to each other.

Referring to Fig. 4, the current global coordinate frame $\{xyz\}$ can be rotated about its y-axis, and, therefore, the action in (12) needs to include a rotation matrix $\boldsymbol{R}_{\mathrm{y}}\ (\varphi)$. Nevertheless, the compliance matrix of the planar spring keeps invariant

$$\boldsymbol{K'}_0 = Ad_{g0}\boldsymbol{K}_0 Ad_{g0}^T \tag{14}$$

where

$$Ad_{g0} = \begin{bmatrix} \boldsymbol{R}_y\left(\varphi\right) & \boldsymbol{0} \\ \boldsymbol{0} & \boldsymbol{R}_y\left(\varphi\right) \end{bmatrix}$$

and it is a 6×6 matrix representation of the special Euclidean group $SE(3)$, which means that $Ad_{g0}^T = Ad_{g0}^{-1}$. Hence, the congruence transformation in (14) is equivalent to a similarity transformation of $\boldsymbol{K}_0$. Considering that $\boldsymbol{K}_0$ is a diagonal matrix, therefore it is an invariant with respect to the similarity transformation, i.e., $\boldsymbol{K'}_0 = \boldsymbol{K}_0$. This reveals the isotropism of this planar spring.

The above proves that this type of planar spring displays the isotropic rotational compliance, which means that a moment about any lines passing through the origin in the xz plane of the global coordinate frame $\{xyz\}$ produces the same angular displacement. This is an attractive characteristic in considering tendon channel arrangements and multiple groups of tendon path for multisegment continuum manipulator. Equation (14) is

$$c_{55} = \frac{2}{3}\cdot\frac{l^3\left(Ad^2+4I_y\right)}{EI_y\left(A\left(5d^2l^2+9d^2r^2-6\sqrt{3}d^2lr+2dl^2r\right)+I_y\left(16l^2+36r^2-24\sqrt{3}lr\right)\right)}.$$

TABLE I
NUMERICAL EXAMPLE OF COMPLIANCE ELEMENTS

Compliance element	Polyethylene
c_{11}	6.23×10^{-5} m/N
c_{22}	3.28×10^{-4} m/N
c_{33}	6.23×10^{-5} m/N
c_{44}	9.54 rad/(N · m)
c_{55}	2.71 rad/(N · m)
c_{66}	9.54 rad/(N · m)

valid for any planar spring configurations that have the diagonal stiffness matrix, and we verify that four-leg and six-leg symmetric configurations possess such isotropic rotational compliance as well.

In the following, we use a numerical example to further reveal the information embodied in the compliance matrix. The dimensions of the planar spring of our prototype are $l = 8$ mm, $b = 1.2$ mm, $h = 1$ mm, $d = 2$ mm, $r = 3.5$ mm. Polyethylene (Young's module $E = 1.1$ GPa and Poisson's ratio $v = 0.42$) is selected as fabrication material (as tabulated in Table I) for use in the example, thus deriving each element of the corresponding numerical compliance matrix.

By analyzing the numerical results, we can draw the following conclusions.

1) In the group of translational compliance elements (c_{11}, c_{22}, and c_{33}), the vertical compliance element c_{22} is about five times larger than both the horizontal compliance element c_{11} along x-axis and the horizontal compliance element c_{33} along z-axis. This result agrees with our intuition and the qualitative study by Howell *et al.* [30]. Such translational motion along the vertical axis of the planar module has been investigated for use in many applications, such as a pneumatic valve controller for Flowserve [30] and a force sensor [40].
2) In the group of rotational compliance elements (c_{44}, c_{55}, and c_{66}), the rotational compliance elements both c_{44} and c_{66} about the horizontal x- and z-axes are more than three times larger than the rotational compliance element c_{55} about the vertical y-axis, indicating its potential to be used for bending motions in continuum manipulator, while resisting in-plane rotations.

Overall, c_{22}, c_{44}, and c_{66} are the major compliance elements. Thus, reasonably, further analysis can focus on the major displacements δ_y, θ_x, and θ_z that are produced by the loads f_y, m_x, and m_z, respectively.

C. FEA Simulations to Validate the Analytical Model

FEA simulation was conducted using the commercial software package (ANSYS 12.0.1 Release). The geometry of a double-layer modular segment model was imported with a SolidWorks geometrical part. The same dimensions and material data were assigned to this simulation study as we noted for the calculations in the previous numerical example. Fig. 5 illustrates the simulation results for two types of loads applied to one layer's central platform, while fixing another layer's central platform. The left line chart depicts the moment–rotation curves of both simulated one layer and double-layer module rotational deflections, where it validates the double-layer module rotation angle doubles the single-layer rotation angle at the same amount of moment. Besides, the line curves indicate that the linear relationships are applicable for the designed module in the range of simulated rotation. Combining the analytical curve of a single-layer model that was previously derived, we can also see that the results agree well with those correspondingly obtained in an FEA simulation. The right line chart indicates the same conclusion in the case of longitudinal displacements. Regarding the minor discrepancy between the analytical prediction and the simulation result, we suspect that it originates from the connection part [intermediate platform, see Fig. 2(a)] between the two parallel beams of each U-shape leg. Because the intermediate platform ideally should be fully rigid, while this part built in FEA simulation possesses the same material properties as the rest of the module.

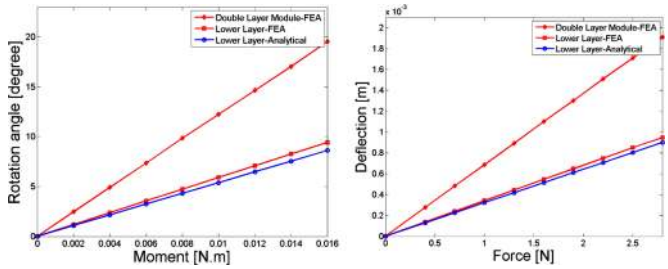

Fig. 5. Moment-rotation diagram (left) and force–deflection diagram (right) for the double-layer compliant module via analytical model predication and FEA simulation results.

In summary, the double-layer compliant module demonstrates an ideal simulation of rotational deflections and longitudinal displacements, which simultaneously can be well predicted with a screw-theory-based analytical model. This simulation verification assures that there are no additional unmodeled effects in the components of the structure that are contributing significantly to the overall system compliance.

IV. ANALYSIS ON THE CONTINUUM MANIPULATOR

A helical spring is commonly used to provide the axial displacement proportional to an applied force in the same direction according to Hooke's law. In this paper, under the framework of the general Hooke's spring law, we analyze another type of springs—planar springs, and for the first time utilize their both translational and angular motions to generate the bending and/or contraction deflections of the continuum manipulator. Before proceeding to the following analysis, there arise two assumptions. One is that the loads exerted on the top plate of the robot are uniformly distributed to each compliant layer. The other is that the frictional effects of tendons are neglected. In the literature, some local spring-based models for continuum robots have been proposed previously in [41] and [42].

A. Compliance of the Robot

The serially connected assembly of multiple layers of planar springs has the compliance attribute equal to the sum of compliance matrix of each layer of the planar spring, i.e., theoretically, $\boldsymbol{C} = n\boldsymbol{C}_0$, where $\boldsymbol{C}$ represents the equivalent compliance of the continuum manipulator in form of a 6×6 diagonal matrix, and n is the total number of planar spring layers. On the other

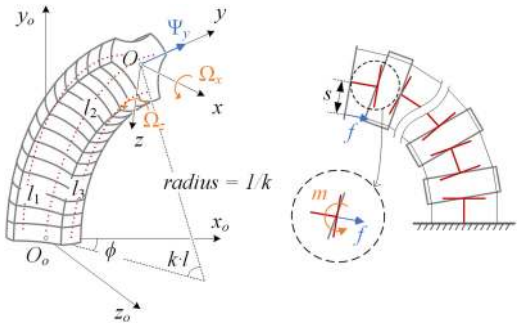

Fig. 6. (a) Configuration of a bending continuum manipulator and its attached coordinate frames; (b) 2-D view of the bending configuration; the zoomed-in view shows the equivalent force and moment acting on the last module when a pulling force is exerted to the top plate via a tendon.

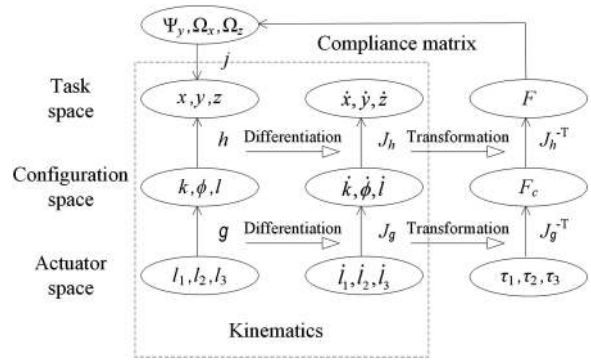

Fig. 7. Overview of kinematic and static relations of the continuum manipulator. The variables in each ellipse represent the chosen mathematical description with respect to the proposed three-tendon driven robot in this paper. l_1, l_2, l_3 are three tendon lengths; *k*, ϕ, *l* are the configuration space variables [*k* is curvature; ϕ is bending angle; *l* is the total length; all the three variables are frequently used in references, all are defined in Fig. 6 (a)]. *x*, *y*, *z* denote the tip position of the continuum manipulator in Cartesian space. F_c is a three-dimensional vector and its elements are related to the corresponding configuration variables. *F* is the effective Cartesian force-moment vector and is represented as the vector $[Fy, Mx, Mz]^T$ in (16). The notation $(\cdot)$ denotes the time derivative.

hand, as we discussed in the end of Section III-C, among the total six compliance elements in (13), only major compliance elements c_{22}, c_{44}, and c_{66} are of our interest. The rest of compliance elements are at relatively small values and can be neglected [37]. Thus, the effectual compliance matrix of the continuum manipulator is

$$\bar{\boldsymbol{C}} = n\bar{\boldsymbol{C}}_0 = \mathrm{diag}\begin{bmatrix} n\cdot c_{22} & n\cdot c_{44} & n\cdot c_{66} \end{bmatrix} \tag{15}$$

where $\bar{\boldsymbol{C}}$, $\bar{\boldsymbol{C}}_0$, respectively, denotes the compliance matrix that only contains three major compliance elements of the robot and a planar spring.

With (15), the following relation between end-point force and robot deflection holds

$$\begin{bmatrix} \Psi_y \\ \Omega_x \\ \Omega_z \end{bmatrix} = \bar{\boldsymbol{C}} \begin{bmatrix} F_y \\ M_x \\ M_z \end{bmatrix} = \begin{bmatrix} n\cdot c_{22} & 0 & 0 \\ 0 & n\cdot c_{44} & 0 \\ 0 & 0 & n\cdot c_{66} \end{bmatrix} \begin{bmatrix} F_y \\ M_x \\ M_z \end{bmatrix} \tag{16}$$

where $[F_y, M_x, M_z]^T$ represents the effective Cartesian force-moment vector on the end-point of the robot; Ω_x, Ω_z are the two rotation angles of the moving frame $\{xyz\}$attached to the end-point of the continuum manipulator, illustrated in Fig. 6(a); particularly, Ψ_y is the change of the total length of the continuum manipulator.

B. Discussions on Bending Deflection Decoupled With Contraction

There are two factors giving rise to the decoupling property that the robot effectively decreases the contraction when generating bending deflections. One is that the compliance matrix in (16) is diagonal. Otherwise, if the entries outside the main diagonal are not all zero, the applied moment intended for the bending deflection will simultaneously generate the contraction (or the compression force will result in bending).

The other is that the rotational compliance has much more significant effects on the robot deflection than the translational compliance. This can be clarified as follows. Assuming a fulling force *f* exerted to the distal plate via the tendon [see Fig. 6(b)], this load is equivalent to a moment $m = f \cdot s$, where *s* is the lever-arm distance to produce the moment of force, and a force *f* acting on upper layer platform of the last module and further being transmitted to the full robot. According to the previous compliance analysis, this moment on the robot will generate a total angular displacement $\Omega = n \cdot c_r \cdot f \cdot s$, and this force will generate a translational displacement $\Psi = n \cdot c_t \cdot f$. ($c_r$ and c_t denote the rotational compliance and translational compliance; referring to Table I, $c_r = 9.54$ rad/(N·m), $c_t = 3.28 \times 10^{-4}$ m/N; in the current robot design, $s = 13.4$ mm, and the total number of planar springs $n = 20$.) Thus, if the exerted force $f = 1$ N, we can calculate $\Omega = 146.5°$ and $\Psi = 0.328$ mm (the total length of the robot is 143 mm). This numerical comparison reveals that when the robot bends to a very large angle, the total contraction of the robot almost remains the same.

Both of the above discussed factors stem from the properties of the planar spring. Other kinds of compliant modules, such as helical springs [14] and pneumatic actuators [27], [28] as reviewed in Section I-A, do not possess this feature that makes the bending deflection of this continuum manipulator effectively decoupled from the contraction.

C. Overview of Continuum Manipulator Kinematics and Statics

We put this continuum manipulator design in the context of continuum robotics. Kinematics and statics of such robots have been widely studied, and review papers can be referred to [1], [10]. As for our three-tendon driven continuum manipulator in this paper, an overview is summarized in Fig. 7, to clarify kinematic relation between tendon lengths and task space variables, and static force relation between tendon tensions and end-point force. For the detailed functions of these kinematic mappings listed in Fig. 7, i.e., submappings *h*, *g*, and their corresponding Jacobians J_h, J_g, see [1], [10], [31], where the same notational convention is employed. Besides, the mapping *j* is derived with the concept of simultaneous rotation and the use of Rodrigues' formula [43], and it is presented in [44].

The kinematic modeling of this continuum manipulator also complies with the constant-curvature approximation [10], and,

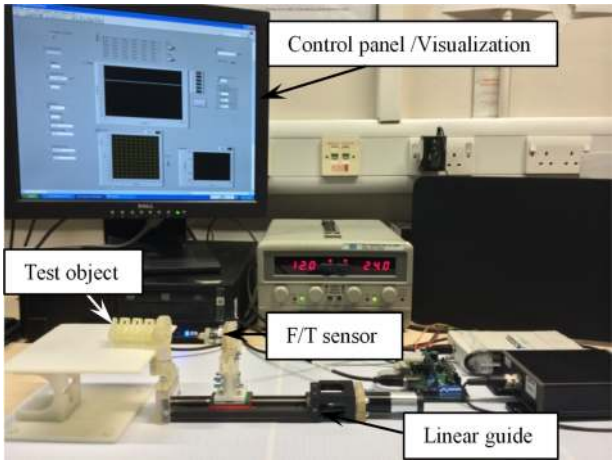

Fig. 8. Experimental setup for modular segment test and quantitative analysis.

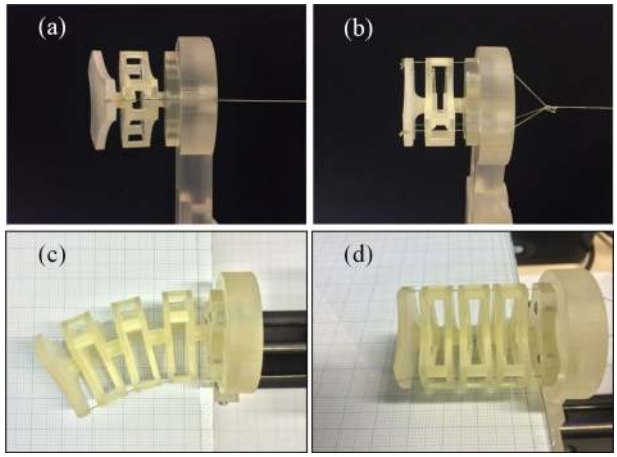

Fig. 9. One modular segment and three-segment assembly, respectively, are mounted to the holder at one side of the linear guide. Forces are exerted via tendon(s): (a) One segment moment-rotation test; (b) one segment contraction test; (c) three-segment assembly moment-rotation test; (d) three-segment assembly contraction test.

thus, the configuration of the backbone can be described by 3-D arc parameters, as given in Fig. 7. In this regards, the static analysis will treat the manipulator as an elastic unit only with three independent DOFs—two rotational DOFs Ω_x, Ω_z and one translational DOF Ψ_y. Here, the robot does not behave as an arbitrarily deformable structure with infinite DOFs [1], [10].

Although the manipulator is supposed to be in the three-tendon actuation manner, one tendon actuation still enables a simple bending deflection, as illustrated in Fig. 6(b). Three-tendon actuation increases the rotational DOF from 2-D to 3-D, and enables the third translational DOF underlying the physical structure. The varying length of the robot results in an enlarged work space, as discussed in the following section. The motion control of the continuum manipulator is commonly conducted by controlling the lengths of tendons to accomplish the tip position tracking tasks with inverse kinematics. Particularly, in our manipulator design, the length of the continuum manipulator can be controllable and further the bending deflection is decoupled from contraction; thus, for each certain length, the tip position can be simply controlled based on the frequently used constant-curvature kinematics [10].

V. Experimental Validation

This section presents experimental results to verify the performance of the proposed continuum manipulator. The experiments validated the cumulative large linear bending characteristic, decoupling property between bending and compression of this continuum manipulator, and its enlarged workspace.

A. Experimental Setup

The double-layer modular segment is made of UV curable acrylic plastic material (VisiJet EX200) and is 3-D printed using a rapid prototyping machine [ProJet HD 3000, Resolution 328 × 328 × 606 DPI (*xyz*)]. Other geometrical dimensions remain the same as before. Modular design here allows the overall length and maximum bending to be easily modified to suit the intended applications.

Fig. 8 shows the experimental test platform and environment, where the double-layer module and the multisegment assembly can be mounted to the holder at one side of a linear guide (KK40-2001, Hiwin). One nonstretchable transmission tendon was routed through the segments and one end terminates at the distal plate (as illustrated in Fig. 3) and another end is fastened to a commercial force sensor (ATI Nano 17 six-DOF force/torque sensor) that is used to record the reaction pull force along the tendon. In order to eliminate the gravity effect, the segment/continuum manipulator was laid on the horizontal plane and only horizontal bending motion is performed via the tendon actuation. The force sensor was held on a moving block attached to the linear guide allowing only linear translation. The taut tendon is always perpendicular to the holding block and corresponds to a consistent moving direction of the slider. The linear guide was driven by a DC motor (Maxon Motor) that was connected to a positioning controller. A LABVIEW program was developed to control the linear guide with the desired speed and to record the reaction force data acquired by the force sensor.

B. Modular Segment Test

The FEA simulation results (see also earlier section) show a highly linear correlation between the twist measurement and the exerted wrench, and agree well with our analytical compliance analysis. Here, the experiments started with single modular segment tests and then three-segment assembly tests. Based on the experimental results, the linear and decoupled behaviors of this multilayer planar spring-based design are further studied. Fig. 9 shows several snapshots of the configurations of a double-layer module and a three-segment assembly when experiencing known loads applied via tendon(s). The other end of the string is tied to the Nano 17 force/torque sensor which is held on the slider and moves along the rail quasi-statically and slowly at a constant speed of 10 mm/min, thus forces are produced along the taut tendons.

1) Results of Segment Bending Test: Fig. 10 illustrates the measured force–displacement curves for the moment loads acting on a double-layer modular segment and a three-segment assembly. A single tendon is utilized in this scenario. Both the *x*- and *y*-values are directly from the collected sensor readouts.

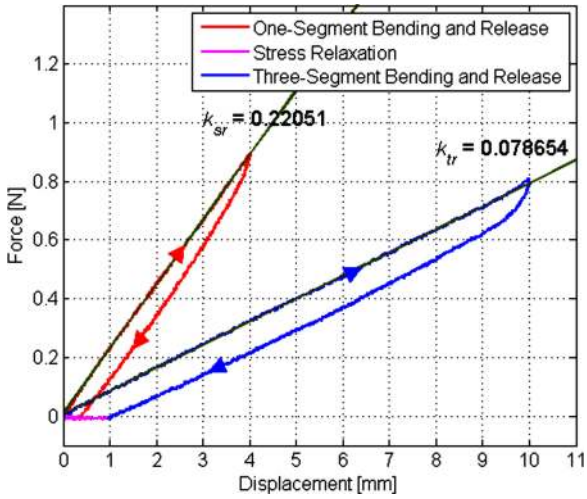

Fig. 10. Plot of experimental results regarding the moment loads on one modular segment and one three-segment assembly. The ATI Nano 17 F/T sensor is adjusted on the holder to allow only one axis force readout along the tendon direction.

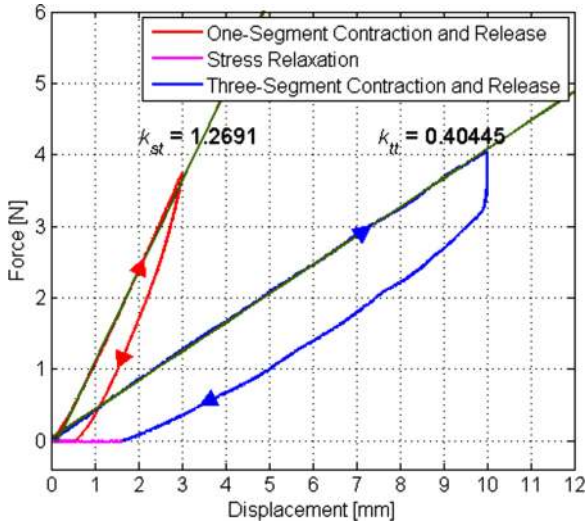

Fig. 11. Plot of experimental results regarding the forces exerted on a segment and a three-segment assembly. The same procedure with the bending tests is followed. The tendon tension is given by the ATI Nano 17 F/T sensor.

The curves are closed loops, revealing the pulling and releasing tendon processes—hysteresis behavior is exhibited. We suspect that the hysteresis is mainly due to material properties and is partly because of the changes in the direction of the friction force. The influence of material properties is a stress relaxation phenomenon where a decrease in stress is observed in response to the same amount of applied strain. In the end of both releasing tendon processes, the total amount of such plastic strain is depicted in magenta in Fig. 10. The single segment relaxation indicated in Fig. 10 is 0.29 mm and it is 7.25% of the total strain measured during this test. The three-segment assembly relaxation is 0.90 mm and it is 9% over the total strain. The increase of stress relaxation is due to the accumulation effect of the multiple segments.

2) Discussions of Segment Bending Test: The forward path corresponding to the pulling tendon process in both one-segment and three-segment tests, as depicted in Fig. 10, displays strong linearity. The reverse path corresponding to the releasing tendon process shows a smooth transition at the very beginning but then exhibits the linear feature. For both tests, the steady slopes of the forward and reverse paths are almost equal. A robust regression technique is utilized to formulate the forward path of each test; the derived slopes k_{sr} for single module test and k_{tr} for three-segment test are labeled in Fig. 10, respectively. It is noted that there exists a multiple relationship between the two slopes ($k_{sr}/k_{tr} \approx 3$), and this matches the fact that the number of segments of the test object has tripled.

This empirical test validates the linearity of the stress–strain relationship. Since the properties of these 3-D printed parts are not completely consistent with the original printing materials, even parts made within the same printing batch exhibit different mechanical performance, thus the comparisons between the experimental and simulation results are not further discussed.

We continue to study the bending configuration of the three-segment assembly in this test and examine its total length. It shows that the maximum coupled contraction is as small as 4% of the original and we can regard the length being invariant. Therefore, these experiments confirm the predicted decoupling between bending and contraction. This is an important aspect and the primary contribution of our multilayer planar spring stacked concept, and, as such, very different from the way helical springs behave. Besides, we observed that each layer's bending angle or contraction distance was about equal and uniformly distributed across the total deformations in all the four tests (see Fig. 9). The maximum reachable bending angle depends on the material properties and segment design.

3) Results of Segment Contraction Test: Fig. 11 shows the measured stress–strain curves for the forces exerted perpendicularly to a double-layer modular segment and a three-segment assembly. Motion snapshots are shown in Fig. 9(b) and (d). In this scenario, three tendons are utilized and they are tied together before they are affixed to the force/torque sensor. The advantage of this is that the test procedure is simplified with only one sensor being needed; however, this approach amplifies the frictional forces between tendons and tendon channels. Since the frictional forces act against the direction of pulling tendons, the reaction forces recorded using the force sensor will be higher than the loads on the test objects. The reverse paths also include the effect of the frictional force but in the different direction, which reduces the tendon tension. In order to reduce the friction, applying the lubrication to tendons and teflon coating and if possible reducing the number of actuated tendons are suggested.

4) Discussions of Segment Contraction Test: The curves in Fig. 11 exhibit the same linear trend as those in Fig. 10; thus, we come to same conclusions as the bending tests in terms of linearity, multiple relation, and hysteresis behavior. The contraction rate here is limited to 80% of the original length and the total relaxation percentage over the total tested contraction is 18.2% for one segment test and 15.9% for the three-segment assembly test. This is much larger than the bending deformation. Using other more homogeneous and low-hysteresis materials, such as aluminum alloy and superelastic NiTi, to fabricate the compliant planar springs can reduce the hysteresis of the modular segment as well as of the assembled continuum body.

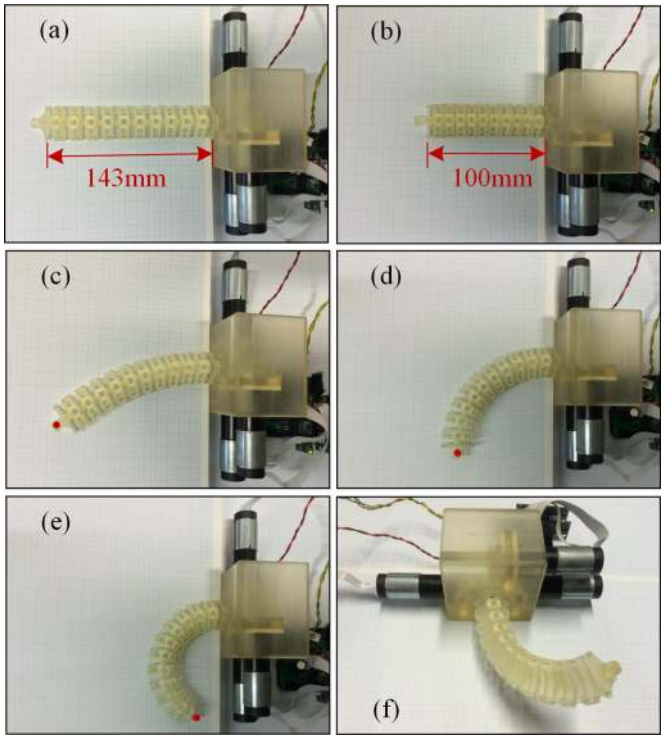

Fig. 12. Proposed continuum manipulator performing bending and contraction deformations. The tip is a mock end effector. (a) Before and (b) after longitudinal contraction; (c)—(e) 2-D bending motion; (f) 3-D bending motion.

C. Continuum Manipulator Prototype Experiments

A 3-D printed prototype of the multilayer structured continuum manipulator was tested; test procedures and results are described in this section. The length of this ten-segment assembled continuum structure is 143 mm and its diameter is 29 mm. Three tendons at the periphery are independently driven by three DC motors (Maxon Motor) with pulleys. The 128:1 reduction gearhead employed allows tendon actuation with a high rotational resolution. The previous three-segment assembly can be used as a flexible robotic tip/wrist, and this continuum manipulator due to its much larger bending and contraction ranges can be used in different scenarios with different end effectors, such as a detachable gripper, sensor module, or cutting tools.

Fig. 12 shows several snapshots of the manipulator's bending and contraction configurations. Fig. 12(a) and (b) presents a comparison of before and after the longitudinal contraction, which indicates the longitudinal compliance, and, to some extent, ensures safety when interacting with the environment. Due to the limited compliance of the fabrication material, the prototype only serves as a preliminary setup for the investigation of the performance of contraction and bending motions. The contraction ratio of the currently fabricated prototype is 0.7, which is determined by material properties, dimensions of the flexible leg segments, and the structure constraints between two adjacent planar springs. On one hand, the longitudinal compliance characteristic is an advantage compared to longitudinally incompressible rod/tube-based continuum manipulators. On the other hand, compared to the helical-spring-backbone-based continuum manipulator, it has the capability of maintaining better structural rigidity for the whole continuum body.

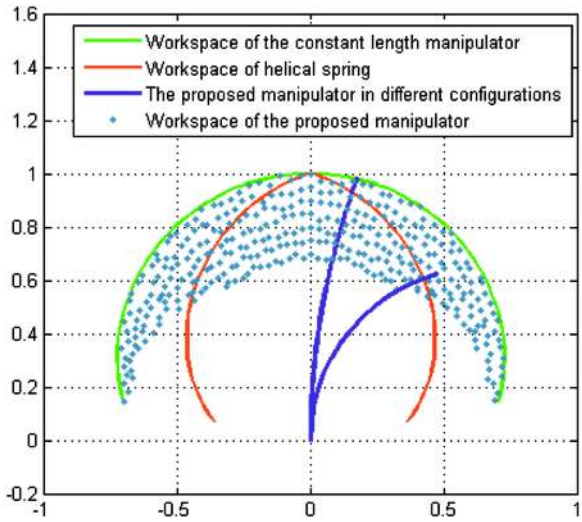

Fig. 13. Normalized workspace of the proposed continuum manipulator compared with constant length and helical-spring-backbone-based continuum manipulators.

TABLE II
EXPERIMENTAL RESULTS FOR DIFFERENT BENDING CONFIGURATIONS

Bending angle	Manipulator length	Contraction
0°	143 mm	0
10°	143 mm	0
20°	143 mm	0
30°	142 mm	0.7%
60°	141 mm	1.4%
90°	140 mm	2.1%
120°	138 mm	3.5%
160°	135 mm	5.6%

Fig. 12(c)–(f) illustrates the bending motion of the manipulator. The continuum manipulator is actuated by three tendons simultaneously and this enables the manipulator to deflect in 3-D space [see Fig. 12(f)]. In order to determine the workspace of the manipulator tip, the 2-D tip positions in the horizontal plane are marked on coordinate paper. The position is later normalized as shown in Fig. 13. Theoretically, the corresponding 3-D workspace is the area of a 2-D workspace swept about its central vertical axis. This results in a large number of possible bending configurations. Several of these configurations were selected for the experiments. The central length of the bending manipulator was then measured for each configuration. The results are listed in Table II. It is noted that the length of the manipulator is almost invariant, however, with the bending angle increasing to values higher than 30° certain levels of contraction are exhibited. The maximum contraction rate is less than 6% and given the fact that the material is nonhomogenous, we can still consider the bending motion to be decoupled from the contraction. The bending and contraction decoupling characteristic makes the design simple to control, while for the helical-spring-backbone-based designs or tendon-driven pneumatic-backbone-based designs, the control effort leading to a bending actuation is partially lost in compression [1]. From Fig. 13, we can see that the red trajectory indicates the tip positions of a spring backbone continuum manipulator when exerted with a bending force.

In Fig. 13, the outermost curve pictured in green indicates the tip trajectory of the continuum manipulator without control efforts to generate compressions. When contracting the manipulator, the bending deflection results in the tip trajectory shrinking to the inner curve layers. Due to the structure constraints, the maximum sweep range of a contracted continuum manipulator is narrowed. It is obvious that the inner curve is always slightly shorter than its adjacent outer curve. All the reachable tip positions form a crescent workspace, which verifies the enlarged workspace compared to a constant length manipulator, for example, a longitudinally incompressible rod/tube-based continuum structure.

VI. Conclusion and Future Work

This paper presented the design of a continuum manipulator with multiple layers of compliant planar modules linked in series. First, we reviewed frequently applied continuum manipulator constructions to date based on the distinctive backbone architecture. Through the study, we found that our structure has advantages over other existing traditional continuum manipulators. These advantages are longitudinal compliance, large linear displacement motions, effectively decoupled contraction, and bending motions, as well as an enlarged workspace.

Second, we derived the compliance matrix of the planar spring and conducted a FEM analysis to further confirm the predicted behavior. Finally, we built and tested a prototype and proceeded with a series of experimental studies. The results verified the claimed characteristics of the manipulator.

Future work will include a broader investigation on different design variations of this type of planar springs as the compliance characteristics of the planar spring are determined by its geometric parameters. We have already noted that changing the U-shape legs' position would enable the design to be more compact, while largely increasing the compliance of the planar spring. Further, we may integrate different designs into one continuum manipulator such that the bending configuration can demonstrate various curvatures as well as various compliances along the continuum manipulator.

Moreover, we will fabricate the continuum manipulator with other materials such as metal; thus, smaller size will be made possible and the hysteresis behavior is expected to be reduced. Kinematic control on this continuum manipulator will be investigated, making fully use of the decoupled bending/contraction feature. Potential applications will be studied with suitable end effectors attached, such as a detachable gripper for medical applications.

References

[1] I. D. Walker, "Continuous backbone 'continuum' robot manipulators," *ISRN Robot.*, vol. 2013, pp. 1–19, 2013.

[2] C. Escande, T. Chettibi, R, Merzouki, V. Coelen, and P. M. Pathak, "Kinematic calibration of a multisection bionic manipulator," *IEEE/ASME Trans. Mechatronics*, vol. 20, no. 2, pp. 663–674, Apr. 2015.

[3] V. C. Anderson and R. C. Horn, "Tensor arm manipulator design," *Trans. ASME*, vol. 67, pp. 1–12, 1967.

[4] S. Hirose, *Biologically Inspired Robots*. London, U.K.: Oxford Univ. Press, 1993.

[5] G. S. Chirikjian, "Hyper-redundant manipulator dynamics: A continuum approximation," *Adv. Robot.*, vol. 9, no. 3, pp. 217–243, 1994.

[6] D. B. Camarillo, T. M. Krummel, and J. K. Salisbury, "Robotic technology in surgery: Past, present, and future," *Amer. J. Surg.*, vol. 188, no. 4A, pp. 2–15, 2004.

[7] T. Kanno, D. Haraguchi, M. Yamamoto, K. Tadano, and K. Kawashima, "A forceps manipulator with flexible 4-DOF mechanism for laparoscopic surgery," *IEEE/ASME Trans. Mechatronics*, vol. 20, no. 3, pp. 1170–1178, 2015.

[8] D. Trivedi, C. D. Rahn, W. M. Kier, and I. D. Walker, "Soft robotics: Biological inspiration, state of the art, and future research," *Appl. Bionics Biomech.*, vol. 5, no. 3, pp. 99–117, 2008.

[9] A. Girard, J.-P. L. Bigue, B. M. O'Brien, T. A. Gisby, I. A. Anderson, and J.-S. Plante, "Soft two-degree-of-freedom dielectric elastomer position sensor exhibiting linear behavior," *IEEE/ASME Trans. Mechatronics*, vol. 20, no. 1, pp. 105–114, Feb. 2015.

[10] R. J. Webster and B. A. Jones, "Design and kinematic modeling of constant curvature continuum robots: A review," *Int. J. Rob. Res.*, vol. 29, no. 13, pp. 1661–1683, 2010.

[11] R. Buckingham, "Snake arm robots," *Ind. Robot.*, vol. 29, no. 3, pp. 242–245, 2002.

[12] C. Wright, A. Johnson, A. Peck, Z. McCord, A. Naaktgeboren, P. Gianfortoni, M. Gonzalez-Rivero, R. Hatton, and H. Choset, "Design of a modular snake robot," in *Proc. IEEE/RSJ Int. Conf. Intell. Robots Syst.*, 2007, pp. 2609–2614.

[13] B. Liao, Z. Li, and R. Du, "Robot tadpole with a novel biomimetic wire-driven propulsor," in *Proc. IEEE Int. Conf. Robot. Biomimetics*, 2012, pp. 557–562.

[14] J. Yang, P. Jason, and K. Abdel-Malek, "A hyper-redundant continuous robot," in *Proc. IEEE Int. Conf. Robot. Autom.*, 2006, pp. 1854–1859.

[15] J. S. Mehling, M. A. Diftler, M. Chu, and M. Valvo, "A minimally invasive tendril robot for in-space inspection," in *Proc. IEEE/RAS-EMBS Int. Conf. Biomed. Robot. Biomechatron.*, 2006, pp. 690–695.

[16] H. Watanabe, K. Kanou, Y. Kobayashi, and M. G. Fujie, "Development of a 'steerable drill' for ACL reconstruction to create the arbitrary trajectory of a bone tunnel," in *Proc. IEEE/RSJ Int. Conf. Intell. Robots Syst.*, 2011, pp. 955–960.

[17] F. Jelínek, E. A. Arkenbout, P. W. J. Henselmans, R. Pessers, and P. Breedveld, "Classification of joints used in steerable instruments for minimally invasive surgery—A review of the state of the art," *J. Med. Device*, vol. 9, no. 1, pp. 010801-1–010801-11, 2015.

[18] I. A. Gravagne, C. D. Rahn, and I. D. Walker, "Large deflection dynamics and control for planar continuum robots," *IEEE/ASME Trans. Mechatronics*, vol. 8, no. 2, pp. 299–307, Jun. 2003.

[19] N. Simaan, "Snake-like units using flexible backbones and actuation redundancy for enhanced miniaturization," in *Proc. IEEE Int. Conf. Robot. Autom.*, 2005, pp. 3012–3017.

[20] D. B. Camarillo, C. F. Milne, C. R. Carlson, M. R. Zinn, and J. K. Salisbury, "Mechanics modeling of tendon-driven continuum manipulators," *IEEE Trans. Robot.*, vol. 24, no. 6, pp. 1262–1273, Dec. 2008.

[21] R. J. Webster, R. Joseph, and N. J. Cowan, "Mechanics of precurved-tube continuum robots," *IEEE Trans. Robot.*, vol. 25, no. 1, pp. 67–78, Feb. 2009.

[22] J. Burgner, D. C. Rucker, H. B. Gilbert, P. J. Swaney, P. T. Russell, K. D. Weaver, and R. J. Webster, "A telerobotic system for transnasal surgery," *IEEE/ASME Trans. Mechatronics*, vol. 19, no. 3, pp. 996–1006, Jun. 2014.

[23] P. E. Dupont, J. Lock, B. Itkowitz, and E. Butler, "Design and control of concentric-tube robots," *IEEE Trans. Robot.*, vol. 26, no. 2, pp. 209–225, Apr. 2010.

[24] Y.-J. Kim, S. Cheng, S. Kim, and K. Iagnemma, "A novel layer jamming mechanism with tunable stiffness capability for minimally invasive surgery," *IEEE Trans. Robot.*, vol. 29, no. 4, pp. 1031–1042, Aug. 2013.

[25] A. Jiang, G. Xynogalas, P. Dasgupta, K. Althoefer, and T. Nanayakkara, "Design of a variable stiffness flexible manipulator with composite granular jamming and membrane coupling," in *Proc. IEEE/RSJ Int. Conf. Intell. Robots Syst.*, 2012, pp. 2922–2927.

[26] M. B. Pritts and C. D. Rahn, "Design of an artificial muscle continuum robot," in *Proc. IEEE Int. Conf. Robot. Autom.*, 2004, pp. 4742–4746.

[27] W. McMahan, V. Chitrakaran, M. Csencsits, D. Dawson, I. D. Walker, B. A. Jones, M. Pritts, D. Dienno, M. Grissom, and C. D. Rahn, "Field trials and testing of the OctArm continuum manipulator," in *Proc. IEEE Int. Conf. Robot. Autom.*, 2006, pp. 2336–2341.

[28] W. M. Kier and K. K. Smith, "Tongues, tentacles and trunks: The biomechanics of movement in muscular-hydrostats," *Zool. J. Linnean Soc.*, vol. 83, no. 4, pp. 307–324, 1985.

[29] P. Qi, C. Qiu, H. Liu, J. S. Dai, L. Seneviratne, and K. Althoefer, "A novel continuum-style robot with multilayer compliant modules," in *Proc. IEEE/RSJ Int. Conf. Intell. Robots Syst.*, 2014, pp. 3175–3180.
[30] J. J. Parise, L. L. Howell, and S. P. Magleby, "Orthoplanar linear-motion springs," *Mechanism Mach. Theory*, vol. 36, no. 11, pp. 1281–1299, 2001.
[31] M. A. Hannan and I. D. Walker, "Kinematics and the implementation of an elephant's trunk manipulator and other continuum style robots," *J. Robot. Syst.*, vol. 20, no. 2, pp. 45–63, 2003.
[32] R. G. Roberts, "Minimal realization of a spatial stiffness matrix with simple springs connected in parallel," *IEEE Trans. Robot. Autom.*, vol. 15, no. 5, pp. 953–958, Oct. 1999.
[33] R. G. Roberts, "Minimal realization of an arbitrary spatial stiffness matrix with a parallel connection of simple and complex springs," *IEEE Trans. Robot. Autom.*, vol. 16, no. 5, pp. 603–608, Oct. 2000.
[34] J. S. Dai, "Finite displacement screw operators with embedded chasles' motion," *J. Mech. Robot.*, vol. 4, no. 4, pp. 041002-1–041002-9, 2012.
[35] J. Selig and X. Ding, "A Screw theory of static beams," in *Proc. IEEE/RSJ Int. Conf. Intell. Robots Syst.*, 2001, vol. 1, pp. 312–317.
[36] X. Ding and J. S. Dai, "Compliance analysis of mechanisms with spatial continuous compliance in the context of screw theory and Lie groups," in *Proc. J. Mech. Eng. Sci.*, vol. 224, no. 11, pp. 2493–2504, 2010.
[37] H.-J. Su, H. Shi, and J. Yu, "A symbolic formulation for analytical compliance analysis and synthesis of flexure mechanisms," *J. Mech. Des.*, vol. 134, pp. 031014-1–031014-12, 2012.
[38] J. S. Dai and X. Ding, "Compliance analysis of a three-legged rigidly-connected platform device," *J. Mech. Des.*,, vol. 128, no. 4, pp. 755–764, 2006.
[39] J. S. Dai, *Geometrical Foundations and Screw Algebra for Mechanisms and Robotics*. Beijing, China: Higher Education Press, 2014 (translated from J.S. Dai, 2017, *Screw Algebra and Kinematic Approaches for Mechanisms and Robotics*, to be published by Springer, London).
[40] A. Ataollahi, A. Fallah, L. Seneviratne, P. Dasgupta, and K. Althoefer, "Novel force sensing approach employing prismatic-tip optical fiber inside an orthoplanar spring structure," *IEEE/ASME Trans. Mechatronics*, vol. 19, no. 1, pp. 121–130, Feb. 2014.
[41] N. Giri and I. D. Walker, "Three module lumped element model of a continuum arm section," in *Proc. IEEE/RSJ Int. Conf. Intell. Robots Syst.*, 2011, pp. 4060–4065.
[42] J. Jung, R. S. Penning, N. J. Ferrier, and M. R. Zinn, "A modeling approach for continuum robotic manipulators: Effects of nonlinear internal device friction," in *Proc. IEEE/RSJ Int. Conf. Intell. Robots Syst.*, 2011, pp. 5139–5146.
[43] J. S. Dai, "Euler-Rodrigues formula variations, quaternion conjugation and intrinsic connections," *Mechanism Mach. Theory*, vol. 92, pp. 134–144, 2015.
[44] P. Qi, H. Liu, L. Seneviratne, and K. Althoefer, "Towards kinematic modeling of a multi-DOF tendon driven robotic catheter," in *Proc. IEEE 36th Annu. Int. Conf. Eng. Med. Biol. Soc.*, Chicago, IL, USA, 2014, pp. 3009–3012.

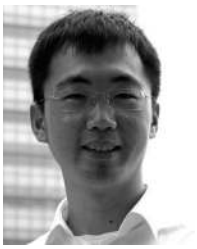

Peng Qi (S'11) received the B.Eng. degree in automation from Beijing Jiaotong University, Beijing, China, in 2010, and the M.S. degree in electrical engineering from the KTH Royal Institute of Technology, Stockholm, Sweden, in 2012. He is currently working toward the Ph.D. degree in robotics at King's College London, London, U.K.

His research interests include design, modeling, and control of continuum/soft manipulators as surgical assistants.

Chen Qiu received the B.S. degree in spacecraft design and engineering from Beihang University, Beijing, China, in 2011. He is currently working toward the Ph.D. degree at the Centre for Robotics Research, King's College London, London, U.K.

His research interests include modeling of robotic stiffness/compliance, design of compliant mechanisms, and soft robots.

Hongbin Liu (M'07) received the B.S. degree from the Northwestern Polytechnique University, Xi'an, China, in 2005, and the M.Sc. degree and Ph.D. degree in robotics from Kings College London, London, U.K., in 2006 and 2010, respectively.

He is currently a Lecturer (Assistant Professor) at the Department of Informatics, King's College London, where he is leading the Robotic Contact Perception Lab. His research interests include tactile/force perception, modeling and control of physical interaction, flexible/continuum medical robots, robotic grasping, and manipulation.

Dr. Liu is a Technical Committee Member for the IEEE EMBS BioRobotics.

Jian S. Dai (SM'02) received the B.Sc. and M.Sc. degrees from Shanghai Jiao Tong University, Shanghai, China, in 1982 and 1984 respectively, and the Ph.D. degree from Salford University, Salford, U.K., in 1993. He is the Chair of Mechanisms and Robotics at the Centre for Robotics Research, King's College London, University of London, London, U.K. He has been working in the field of mechanisms and robotics in the past 26 years and published more than 450 peer-reviewed papers including 230 journal papers and four books. His research interests include theoretical and computational kinematics, reconfigurable mechanisms, dexterous mechanisms and manipulators, end effectors, and multifingered hands.

He is a Fellow of the ASME and a Fellow of the IMechE. He received the 2015 ASME Mechanisms and Robotics Award as the 27th recipient since this prestigious lifelong contribution award was established in 1974. He also received several journal and conference best paper awards, the ASME outstanding contribution award as the Conference Chair of the 36th ASME mechanisms and robotics conference held in Chicago, the 2012 Overall Supervisory Excellence Award by King's College London, and the 2012 Mechanism Innovation Award by China Mechanisms Committee. He is currently a Subject Editor of the *Mechanism and Machine Theory*, an Associate Editor of the *ASME Transactions: Journal of Mechanisms and Robotics,* and was an Associate Editor of the IEEE TRANSACTIONS ON ROBOTICS.

Lakmal D. Seneviratne received the Ph.D. degree in Engineering Mechanics from King's College London, U.K., in 1985. He was a Professor of mechatronics at Kings College London, London, U.K., where he was the Founding Director with the Centre for Robotics. He is currently an Associate VP for Research and the Director at the Robotics Institute, Khalifa University, Abu Dhabi, UAE. He has published more than 300 peer-reviewed research papers related to robotics.

Kaspar Althoefer (M'01) received the Ph.D. degree from King's College London, London, U.K., in 1996.

In 1996, he joined the Department of Mechanical Engineering, King's College London, as a Lecturer, where he is currently a Professor of robotics and intelligent systems at the Department of Informatics and the Head at the Centre for Robotic Research. His current research interests include force and tactile sensors for medical applications, miniaturized optic-fiber-based sensing, medical robotics, soft and continuum robots, and neurofuzzy sensor signal analysis and classification.